18 Terabit/s photonic digital signal processor for real time video images

David Moss

HAL Id: hal-03764244
https://hal.science/hal-03764244

Preprint submitted on 30 Aug 2022

18 Terabit/s photonic digital signal processor for real time video images

David J. Moss

Optical Sciences Centre, Swinburne University of Technology, Hawthorn, VIC 3122, Australia

Digital signal processing has become central to many fields, from coherent optical telecommunications where it is used to compensate signal impairments, to video image processing. Image processing in particular is important for observational astronomy, medical diagnosis, autonomous driving, big data and particularly artificial intelligence. Digital signal processing is mainly performed electronically, but new applications, particularly those involving real time video image processing, are creating unprecedented demand for ultrahigh performance, including bandwidth and reduced energy consumption. Here, we demonstrate a photonic digital signal processor operating at 18 Terabits/s and use it to process multiple simultaneous video signals in real-time. The system processes 400,000 video signals concurrently, performing 34 functions simultaneously that are key to object edge detection, edge enhancement and motion blur. As compared with spatial-light devices used for image processing, our system is not only ultra-high speed but highly reconfigurable and programable, able to perform many different functions without any change to the physical hardware. Our approach, based on an integrated Kerr soliton crystal microcomb, opens up new avenues for ultrafast robotic vision and machine learning.

Image processing, the application of signal processing techniques to photographs or videos, is a core part of emerging technologies such as machine learning and robotic vision, [1]with applications to LIDAR for self-driving cars [2], remote drones [3], automated in-vitro cell-growth tracking for virus and cancer analysis [4], optical neural networks [5], ultrahigh speed imaging [6, 7], holographic three-dimensional (3D) displays [8-9], and many others. Many of these require real-time processing of massive real-world information, placing extremely high demands on the processing speed (bandwidth) and throughput of image processing systems. While electrical digital signal processing (DSP) technologies [10] are well established, they face intrinsic limitations in processing speed such as the well-known von Neumann bottleneck [11].

Optical image processing offers the potential for much higher speeds [2], and optical analog computing, for functions such as edge detection of static images using spatial signal differentiation for example, have been achieved using silicon photonic crystal metasurfaces [12], surface plasmonic structures [13], and topological interfaces [14]. These free-space, spatial-light devices offer many attractions such as compact footprint, low power consumption, and compatibility with commercial cameras and optical microscopes. However, they tend to be non-reconfigurable fixed systems designed to perform a single function. On a more advanced level, human action recognition through processing of video image data, has been achieved using photonic computers [15, 16]. However, these were achieved either in comparatively low speed systems [15] or in high bandwidth (multi-TeraOP regime) systems but based on bulk-optics inconducive to integration [16]. To date, optical systems, especially those compatible with integration, [17] still have not demonstrated processing of large data sets of high-definition video images at ultra-high speeds – enough for real-time video image processing.

Here, we demonstrate an optical real-time digital signal processor for digital video images that is reconfigurable, is based on components that are either integrated or compatible with integration, and operates at ultra-high bandwidths of 18 Terabits/s. This is sufficient to process almost 400,000 (399,061) video signals concurrently and in real-time, with up to 34 functions simultaneously. The system is equivalent to electrical digital signal processing (DSP) systems but performs at multi-terabit/s bandwidths, enabled by massively parallel processing. It is also very general, flexible, and highly reconfigurable – able to perform a wide range of functions without requiring any change in hardware. We perform multiple image processing functions in real-

time, which is essential for machine vision and microscopy for tasks such as object recognition or identification, feature capture, and data compression [12-13]. These functions include edge enhancement, edge detection, and motion blur correction. Edge enhancement and detection are key approaches to object recognition that rely on the detection of edges, or discontinuities in image brightness, texture, colour, or other properties. The processes that we employ to perform these functions include Hilbert transforms and differentiation for object edge enhancement and detection, and include both integral order and a continuous range of fractional order transforms, as well as image integration for motion blur.

We demonstrate operation with 34 different functions, although the range of different functions is in fact unlimited given that the system can process a continuous range of arbitrary order functions, including fractional-order to high order differentiation, for example. Our system uses an integrated Kerr microcomb source that generates 95 discrete taps, or wavelengths as the basis for massively parallel processing, with single channel rates at 64 GigaBaud (pixels/s). The experimental results agree well with the theory, demonstrating that the processor is a powerful approach for ultrahigh-speed video image processing for robotic vision, machine learning, and many other emerging applications.

Principle of Operation

Figure 1 illustrates the operational principle of the video image processor, which is based on the principle of an RF photonic transversal filter [18]. The input digital video image frames were first flattened into a vector X and encoded as the intensities of temporal symbols in a serial electrical waveform with a resolution of 8 bits per symbol at a sampling rate of 64 gigabaud. After digital-to-analogue conversion, the generated electrical waveform was multi-cast via electro-optical modulation onto comb lines of a Kerr microcomb, weighted by the calculated function-dependent tap coefficients. The modulated optical signal was then transmitted through a spool of single mode fibre (SMF) to generate a relative delay between different comb lines (wavelength channels). The delayed replicas contained in the wavelength channels were then summed upon photodetection and lastly, the generated RF signal was resampled and converted back to digital video image frames, which formed the output signal of the system. The transfer function of the system is given by

$$H(\omega) = \sum_{n=0}^{N-1} h(n)e^{-j\omega nT} \tag{1}$$

where ω is the RF angular frequency, T is the time delay between adjacent taps (i.e., wavelength channels), and $h(n)$ is the tap coefficient of the nth tap, or wavelength, which can be calculated by performing the inverse Fourier transform of $H(\omega)$ [19-20]. In Eq. (1), the tap coefficients can be tailored by shaping the power of comb lines according to the different computing functions (e.g., differentiation, integration, and Hilbert transformation), thus enabling different video image processing functions. For microcombs with multiple equally spaced comb lines transmitted over the dispersive SMF, in Eq. (1) T is given by $T = D \times L \times \Delta\lambda$, where D is the dispersion coefficient of the SMF, L is the length of the SMF, and $\Delta\lambda$ is the spectral range between adjacent comb lines. In our case, we used standard SMF with D = ~17 ps/nm/km.

The real-time video image processing system is based on a soliton crystal (SC) microcomb source, generated in an integrated MRR (Extended Data Figure 1). Since their first demonstration in 2007 [21], optical frequency combs generated by compact micro-scale resonators, or micro-combs [22-25], have led to significant breakthroughs in a variety of different fields such as metrology [26], spectroscopy [25, 27], telecommunications [23, 28], quantum optics [29-30], and radio-frequency (RF) photonics [18-20, 31-32]. In the field of RF photonics, microcombs not only offer new possibilities for conventional RF signal processing [18-19, 33-34], but have also enabled major advances in emerging applications such as optical neural networks [5], frequency synthesis [35], and light detection & ranging (LIDAR) [2, 36-37]. With a good balance between gain and cavity loss as well as dispersion and nonlinearity, soliton microcombs feature high coherence and low phase noise and have been highly successful at RF photonic applications [19, 38].

SC microcombs, multiple self-organized solitons [39], have been highly successful for RF photonic signal processing [19, 38, 40-44], ultra-dense optical data transmission [23], and optical neuromorphic processing [5, 45]. They feature very high coherence with low phase noise [44], are intrinsically stable with only open-loop control (Supplementary Fig. S2 and supplementary Movie S1) and can be simply and reliably initiated via

manual pump wavelength sweeping. Further, they have intrinsically high conversion efficiency since the intra-cavity energy is much higher than for single soliton states [5]. Our microcomb has a low free spectral range (FSR) of ~48.9 GHz which generates over 80 wavelengths in the telecom C-band, which serves as discrete taps for the video image processing system.

We experimentally demonstrate video image processing in real time, with 34 functions performed simultaneously for edge enhancement, edge detection, and motion blur. Edge detection forms the basis for object detection, feature capture, and data compression [12-13]. Here, we achieve this by spatial signal differentiation with either high integral or fractional order derivatives that extract information about object boundaries in images or videos. We also perform a motion blur function based on signal integration that represents the apparent streaking of moving objects in images or videos. It usually occurs when the image being recorded changes during the recording of a single exposure, and has wide applications in computer animation and graphics [46]. Edge enhancement, or sharpening, based on signal Hilbert transformation is also a fundamental processing function with wide applications [47]. It enhances the edge contrast of images or videos, thus improving their acutance. These processing functions not only underpin conventional image or video processing [48-49] but also facilitate emerging technologies such as robotic vision and machine learning [2, 4].

A key feature of our system that was critical in achieving high fidelity and high performance signal processing was the improvement we obtained in the frequency comb spectral line shaping accuracy. To accomplish this we employed a two-stage shaping strategy (see methods) [50] where a feedback control path was employed to calibrate the system and further improve the comb shaping accuracy. Here, the error signal was generated by directly measuring the impulse response of the system and then comparing it with ideal tap coefficients. Note that this type of feedback calibration approach is challenging and rarely used for analog optical signal computing, such as the systems based on either spatial-light meta-surfaces [12, 51] or waveguide resonators [35, 52], for example.

Experimental Results – Static Images

Figure 2 shows the experimental results of static image processing using the above RF photonic system. The original (unprocessed) high definition (HD) digital images had a resolution of 1080 × 1620 pixels. The results for edge detection based on signal differentiation with orders of 0.5, 0.75, and 1 are shown in Figs. 2(a) – (c), respectively. In each figure, we show (i) the designed and measured spectra of the shaped comb, (ii) the measured and simulated spectral response, and (iii) the measured and simulated images after processing. The measured comb spectra and spectral response were recorded by an optical spectrum analyser (OSA) and a vector network analyser (VNA), respectively. The experimental results agree well with theory, indicating successful edge detection for the original images.

In Figs. 2(d) – (f), we show the results for motion blur based on signal integration with different tap numbers of 15, 45, and 75, respectively. These are also in good agreement between the experimental results and theory. The blur intensity increases with the increased number of taps, reflecting the fact that there is improved processing performance as the number of taps increases. Compared with discrete laser arrays that suffer from relatively bulky size which limits the number of available taps, microcombs generated by a single MRR can operate as a multi-wavelength source that provides a large number of wavelength channels, as well as greatly reducing the size, power consumption, and complexity. This is very attractive for the RF photonic transversal filter system that requires a large number of taps for improved processing performance.

Figs. 2(g) – (I) show the results of edge enhancement based on signal Hilbert transformation (90° phase shift) with different operation bandwidths of 12 GHz, 18 GHz, and 38 GHz, respectively. In our experiment, the operation bandwidth was adjusted by changing the comb spacing (2 FSRs vs 3 FSRs of the MRR) and the fibre length (1.838 km vs 3.96 km). Note that having to change the fibre length in principle can be avoided by using tunable dispersion compensators [53-54]. As can be seen, the edges in the images are enhanced, and the experimental results are consistent with the simulations.

We also demonstrate more specific image processing such as edge detection based on fractional differentiation with different orders of 0.1 – 0.9, edge enhancement based on fractional Hilbert transformation with different phase shifts of 15° – 75°, and edge detection with different operation bandwidths of 4.6 GHz – 36.6 GHz (Supplementary Fig. S3 – S6). By changing the relevant parameters, this resulted in processed images with

different degrees of edge detection, motion blur, and edge enhancement. By simply programming the WaveShaper to shape the comb lines according to the designed tap coefficients, different image processing functions are realized without changing the physical hardware. This reflects the high reconfigurability of our video image processing system, which is challenging for image processing based on spatial-light devices [12-14]. In practical image processing, there doesn't exist a single processing function that has one set of parameters that can meet all the requirements. Rather, each processing function requires its own unique set of tap weights. Hence, the high degree of reconfigurability and versatility of our image processing system is critical to meet diverse and practical processing requirements.

Experimental Results – Real-Time Video

In addition to static image processing, our microcomb based RF photonic system can also be used to process dynamic videos in real-time. Our results for real-time video processing are provided in supplementary Movie S2, while the Extended Data Figures show samples of these experimental results. The supplementary Movie S2. starts off with the first original source video frames and is followed by the simulation and experiment results shown side by side for the differentiator, integrator, and Hilbert transformer. This is then followed by the 34 functions (Table S1) performed simultaneously by the massively parallel video processor. Finally, the results for high order derivatives are shown, and the video finishes with results showing full 2 dimensional derivatives (see below).

The first original video had a resolution of 568 × 320 pixels and a frame rate of 30 frames per second. Extended Data Figure 2(a) shows 5 frames of the original video, together with the corresponding electrical waveform after digital-to-analogue conversion. Extended Data Figure 2(b) – (d) show the corresponding results for the processed video after edge detection (0.5-order fractional differentiation), motion blur (integration with 75 taps), and edge enhancement based on a Hilbert transformation with an operation bandwidth of 18 GHz, respectively. As for the static image processing, the real-time video processing results show good agreement with theoretical predictions.

To fully exploit the bandwidth advantage of optical processing, we further performed massively parallel real-time multi-functional video processing. The experimental setup and results are shown in Fig. 3. We used 95 comb lines around the C band in our demonstration. After flattening and splitting the comb lines via the first WaveShaper, we obtained 34 parallel processors, most of which consisted of five taps. We simultaneously performed 34 video image processing functions, including fractional differentiation with fractional order from 0.05 to 1.1, fractional Hilbert transformation with phase shift from 65° to 90°, an integrator, and bandpass Hilbert transformation with a 90° phase shift (see Supplementary and Table S1 for detailed parameters for each function). The corresponding total processing bandwidth equals 64 GBaud $\times$ 34 (functions) $\times$ 8 bits = 17.4 Terabit/s – well beyond that of electrical video image processors [10].

Discussion

To analyze the performance of our video image processor, we evaluated the processed images based on the ground truth for both quantitative and qualitative comparisons [55]. We used respective ground truths for the evaluation of 3 BSD (Berkeley Segmentation Database) images after edge detection and compared relevant performance parameters with the same images processed based on the widely used Sobel's algorithm [56]. Fig. 4 shows the images processed using Sobel's algorithm and our video image processor (including differentiation with different orders from 0.2 to 1.0). The comparison of the performance parameters including performance ratio (PR) and F-Measure is provided in Table 1, where higher values of these parameters reflect a better edge detection performance. As can be seen, our differentiation results for PR and F-Measures are better than Sobel's approach, reflecting the high performance of our video image processor.

The maximum input rate we used was 64 GBaud, or Gigapixels/s. This, combined with the fact that we performed 34 channels with a video resolution of 568 × 320 that resulted in 181,760 pixels at a frame rate of 30 Hz, yields simultaneous real-time processing of $64 \times 10^9 \times 34/ 5,452,800 = 399,061$ video signals per second. For HD videos (720 × 1280 = 921,600 pixels) at a frame rate of 50 Hz, this equates to about 47,222 video signals in parallel. The processing throughput can be increased even further by using more comb lines in the L-band.

The processing accuracy of our system is lower than electrical DSP image processing but higher than analog image processing based on passive optical filters [13, 52, 57] (see Supplementary Fig. S7 and Table S1). This is mainly a result of the hybrid nature of our system, which is equivalent to electrical DSP systems but

implemented by photonic hardware. There are a number of factors that can lead to tap errors during the comb shaping, thus leading to a non-ideal frequency response of the system as well as deviations between the experimental results and theory. These mainly include a limited number of available taps, the instability of the optical microcomb, the accuracy of the WaveShapers, the gain variation with wavelength of the optical amplifiers, the chirp induced by the optical modulator, the second-order dispersion (SOD) induced power fading, and the third-order dispersion (TOD) of the dispersive fibre.

The number of available taps can be increased by using MRRs with smaller FSRs or optical amplifiers with broader operation bandwidths. The accuracy realized by the WaveShapers and the optical amplifiers was significantly improved by using a two-stage comb shaping strategy as well as the feedback loop calibration mentioned previously. [50] By using low-chirp modulators, the chirp-induced tap errors can be suppressed. The discrepancies induced by the SOD and TOD of the dispersive fibres can also be reduced by using a second WaveShaper to compensate for the group delay ripple of the system (see Supplementary Fig. S8).

Our massively parallel photonic video image processor, which operates on the principle of time-wavelength-spatial multiplexing, similar to the optical vector convolutional accelerator in our previous work [5], is also capable of performing convolution operations for deep learning neural networks. This opens up new opportunities for image or video processing applications in robotic vision and machine learning. In particular, each parallel function can be trained and performed as many as 34 kernels with a size of 5 by 1 for the convolutional neural network, therefore could ultimately achieve a neural network, avoiding the bandwidth limitation given by the analogue-to-digital converters.

Although the experiments reported here included benchtop components, such as the commercially available WaveShaper, there is strong potential for much higher levels of integration, even reaching full monolithic integration. The core component of our system, the microcomb, is already fully integrated. Further, all of the other components have been demonstrated in integrated form, including integrated InP spectral shapers [54], high-speed integrated lithium niobite modulators [58], integrated dispersive elements [59], and photodetectors [60]. Finally, low power consumption and highly efficient microcombs have been demonstrated with single soliton states [61] and laser cavity-soliton Kerr combs [62 - 65], which would greatly reduce the energy requirements. The laser cavity-soliton microcombs as well as the early work based on 200GHz semi-coherent combs [18-20, 33,34, 66-68] and later on soliton crystals [5, 23, 40-45, 50, 69-80] have been based on the Hydex platform, [22, 24, 52, 81-95] which has proven to be extremely successful both for these classical processes as well as quantum optics. [96-104] Recently, [ ] progress has been made on microcombs realized in low temperature (annealing free) CMOS compatible silicon nitride ring resonators. [105] Finally, many functions such as dispersion and time delays can be realized with much more compact devices such as etalon based dispersion compensators. [106, 107]

In conclusion, we report the first demonstration of video image processing based on Kerr microcombs. Our RF photonic processing system, with an ultrahigh processing bandwidth of 17.4 Tbs/s, can simultaneously process over 399,061 video signals in real-time. The system is highly reconfigurable via programmable control, and can perform different processing functions without changing the physical hardware. We experimentally demonstrate different video image processing functions including edge detection, motion blur, and edge enhancement. The experimental results agree well with the theory, verifying the effectiveness of using Kerr microcombs for ultrahigh-speed video image processing. Our results represent a significant advancement for fundamental photonic computing, paving the way for practical ultrahigh bandwidth real-time photonic video image processing on a chip.

The authors declare no competing interests

References

[1] Petrou M, Bosdogianni P, Image processing: the fundamentals. John Wiley (1999)

[2] J. Riemensberger, A. Lukashchuk, M. Karpov, W. Weng, E. Lucas, J. Liu, T. J. Kippenberg, "Massively parallel coherent laser ranging using a soliton microcomb", *Nature* **581** (7807), 164-170 (2020).

[3] Hodge, V.J., Hawkins, R. & Alexander, R. Deep reinforcement learning for drone navigation using sensor data. *Neural Comput & Applic* **33**, 2015–2033 (2021).

[4] Fusciello, M., Fontana, F., Tähtinen, S. et al. Artificially cloaked viral nano-vaccine for cancer immunotherapy. *Nat Commun* **10**, 5747 (2019).

[5] X. Xu, M. Tan, B. Corcoran, J. Wu, A. Boes, T. G. Nguyen, S. T. Chu, B. E. Little, D. G. Hicks, R. Morandotti, A. Mitchell, D. J. Moss, "11 TOPS photonic convolutional accelerator for optical neural networks", *Nature* vol. **589,** 44-51 (2021).

[6] P. Wang, J. Liang, & L.V. Wang, "Single-shot ultrafast imaging attaining 70 trillion frames per second", *Nature Communications* (2020). https://doi.org/10.1038/s41467-020-15745-4

[7] L. Gao, J. Liang, C. Li, L.V. Wang, "Single-shot compressed ultrafast photography at one hundred billion frames per second", *Nature* **516** (7529), 74-77 (2014).

[8] K. Wakunami, P. Hsieh, R. Qi, T. Senoh, H. Sasaki, Y. Ichihashi, M. Okui, Y. Huang, and K. Yamamoto, "Projection-type see-through holographic three-dimensional display", *Nat. Commun.* **7**, 12954 (2016).

[9] S. Tay, et al., "An updatable holographic three-dimensional display", *Nature* **451**, 694-698 (2008).

[10] Gonzalez, Rafael, Digital image processing. New York, NY: Pearson. ISBN 978-0-13-335672-4. OCLC 966609831, (2018).

[11] Backus, John, "Can Programming Be Liberated from the von Neumann Style? A Functional Style and Its Algebra of Programs" (PDF). Communications of the ACM. Vol. 21, No. 8: 613–641. Retrieved September 19, 2020 – via Karl Crary, School of Computer Science, Carnegie Mellon University, (August 1978).

[12] Y. Zhou, H. Zheng, I. I. Kravchenko, and J. Valentine, "Flat optics for image differentiation," *Nature Photonics* **14**, 316-323 (2020).

[13] T. Zhu, Y. Zhou, Y. Lou, H. Ye, M. Qiu, Z. Ruan, and S. Fan, "Plasmonic computing of spatial differentiation," *Nature Communications* **8**, 15391 (2017).

[14] T. Zhu, C. Guo, J. Huang, H. Wang, M. Orenstien, Z. Ruan, and S. Fan, "Topological optical differentiator," *Nature Communication* **12**, 680 (2021).

[15] P. Antonik, N. Marsal, D. Brunner, and D. Rontani, "Human action recognition with a large-scale brain-inspired photonic computer", *Nature Machine Intelligence* **1**, 530-537 (2019).

[16] T. Zhou, X. Lin, J. Wu, Y. Chen, H. Xie, Y. Li, J. Fan, H. Wu, Lu. Fang, and Q. Dai, "Large-scale neuromorphic optoelectronic computing with a reconfigurable diffractive processing unit", *Nature Photonics* **15**, 367-373 (2021).

[17] F. Ashtiani, A. J. Geers, and F. Aflatouni, "An on-chip photonic deep neural network for image classification", *Nature*, June 1, (2022). DOI: 10.1038/s41586-022-04714-0.

[18] X. Xu et al. Reconfigurable broadband microwave photonic intensity differentiator based on an integrated optical frequency comb source. *APL Photonics* **2**, 096104 (2017).

[19] J. Wu et al., "RF photonics: An optical micro-combs' perspective", *IEEE Journal of Selected Topics in Quantum Electronics* **24**, (4), 1-20, Article: 6101020 (2018).

[20] X. Xu, M. Tan, J. Wu, R. Morandotti, A. Mitchell and D. J. Moss, Microcomb-based photonic RF signal processing. *IEEE Photonics Technology Letters* **31**, 1854-1857 (2019).

[21] P. Del'Haye, A. Schliesser, O. Arcizet, T. Wilken, R. Holzwarth, and T. J. Kippenberg, "Optical frequency comb generation from a monolithic microresonator", *Nature* **450**, 1214-1217 (2007).

[22] D. J. Moss, R. Morandotti, A. L. Gaeta, M. Lipson, New CMOS-compatible platforms based on silicon nitride and Hydex for nonlinear optics. *Nature photonics* **7**, 597 (2013).

[23] B. Corcoran et al., "Ultra-dense optical data transmission over standard fiber with a single chip source", *Nature Communications* vol. **11,** 2568 (2020).

[24] Pasquazi, A. et al. Micro-combs: A novel generation of optical sources. *Physics Reports* vol. **729**, 1-81 (2017).

[25] T. J. Kippenberg, R. Holzwarth, S. A. Diddams, Microresonator-based optical frequency combs. *Science* **332**, 555-559 (2011).

[26] Brasch, V. et al. Photonic chip–based optical frequency comb using soliton Cherenkov radiation. *Science* **351**, 357–360 (2016).

[27] Suh, M.-G., Yang, Q.-F., Yang, K. Y., Yi, X. & Vahala, K. J. Microresonator soliton dual-comb spectroscopy. *Science* **354**, 600–603 (2016).

[28] Marin-Palomo, P. et al. Microresonator-based solitons for massively parallel coherent optical communications. *Nature* **546**, 274–279 (2017).

[31] Del'Haye, P. et al. Phase-coherent microwave-to-optical link with a self-referenced microcomb. *Nat. Photonics* **10**, 516-520 (2016).

[32] Liang, W., Eliyahu, D., Ilchenko, V. S., Savchenkov, A. A., Matsko, A. B., Seidel, D., & Maleki, L. High spectral purity Kerr frequency comb radio frequency photonic oscillator. *Nat. Commun.* **6**, 7957 (2015).

[33] X. Xu, et al., "Advanced RF and microwave functions based on an integrated optical frequency comb source", *Opt. Express* vol. **26**, 2569-2583 (2018).

[34] X. Xu, et al., "Broadband RF channelizer based on an integrated optical frequency Kerr comb source", *Journal of Lightwave Technology* vol. **36**, 4519-4526 (2018).

[35] Spencer, D. T. et al. An Optical-Frequency Synthesizer Using Integrated Photonics, *Nature* **557**, 81-85 (2018).

[36] Trocha, P. et al. Ultrafast optical ranging using microresonator soliton frequency combs. *Science* **359**, 887-891 (2018).

[37] Suh, M.-S. & Vahala, K. J. Soliton microcomb range measurement. *Science* **359**, 884-887 (2018).

[38] T. J. Kippenberg, A. L. Gaeta, M. Lipson, and M. L. Gorodetsky, "Dissipative Kerr solitons in optical microresonators", *Science* **361**, 567 (2018).

[39] Z. Lu et al., "Synthesized soliton crystals", *Nature Communication* **12** (1), 1-7 (2021).

[40] M. Tan et al., "Microwave and RF photonic fractional Hilbert transformer based on a 50 GHz Kerr micro-comb", *J. Lightwave Technol.* **37** (4), 6097-6104 (2019).

[41] X. Xu et al., "Advanced adaptive photonic RF filters with 80 taps based on an integrated optical micro-comb source", *J. Lightwave Technol.* **37** (24), 1288-1295 (2019).

[42] M. Tan et al., "Photonic RF arbitrary waveform generator based on a soliton crystal micro-comb source", *J. Lightwave Technol.* vol. **38** (22), 6221-6226 (2020).

[43] X. Xu et al., "Photonic RF and microwave integrator based on a transversal filter with soliton crystal microcombs", *IEEE Transactions on Circuits and Systems II: Express Briefs* vol. **67** (12), 3582-3586 (2020).

[44] X. Xu et al., "Broadband microwave frequency conversion based on an integrated optical micro-comb source", *Journal of Lightwave Technology* vol. **38** (2), 332-338 (2020).

[45] X. Xu, M. Tan, B. Corcoran, J. Wu, T. G. Nguyen, A. Boes, Sai. T. Chu, B. E. Little, R. Morandotti, A. Mitchell, D. G. Hicks, and D. J. Moss, "Photonic Perceptron Based on a Kerr Microcomb for High-Speed, Scalable, Optical Neural Networks", *Laser & Photonics Reviews*, vol. **14** (10), 2000070 (2020).

[46] H. Ji, C. Q. Liu, "Motion blur identification from image gradients", *CVPR* (2008).

[47] J. A. Davis, D. E. McNamara, and D. M. Cottrell, "Analysis of the fractional Hilbert transform," *Appl. Opt.* **37** (29), 6911-6913 (1998).

[48] J. Capmany, J. Mora, I. Gasulla, J. Sancho, J. Lloret, and S. Sales, "Microwave Photonic Signal Processing," *Journal of Lightwave Technol.* **31,** (4), 571-586 (2013).

[49] T. Yang, J. Dong, L. Liu, S. Liao, S. Tan, L. Shi, D. Gao, and X. Zhang, "Experimental observation of optical differentiation and optical Hilbert transformation using a single SOI microdisk chip," *Scientific Reports* **4**, 3960 (2014).

[50] M. Tan, et al., "Integral order photonic RF signal processors based on a soliton crystal micro-comb source", *Journal of Optics* vol. **23** (12), 125701 (2021)

[51] F. Zangeneh-Nejad, D. L. Sounas, A. Alù, and R. Fleury, "Analogue computing with metamaterials", *Nature Reviews Materials* **6**, 207-225 (2020).

[52] M. Ferrera, et al., "On-chip CMOS-compatible all-optical integrator", *Nat. Commun.* vol. **1**, 29 (2010).

[54] A. J. Metcalf, et al., "Integrated line-by-line optical pulse shaper for high-fidelity and rapidly reconfigurable RF-filtering," *Optics Express* **24** (21), 23925-23940 (2016).

[55] P. A. Khaire, and N. V. Thakur, "A Fuzzy Set Approach for Edge Detection", *International Journal of Image Processing (IJIP)* **6** (6), 403-412 (2012).

[56] T. Shi, J. Kong, X. Wang, Z. Liu, and G. Zheng, "Improved Sobel algorithm for defect detection of rail surfaces with enhanced efficiency and accuracy", *J. Cent. South Univ.* **23**, 2867–2875 (2016).

[57] F. F. Liu, et al., "Compact optical temporal differentiator based on silicon microring resonator", *Opt. Express* **16**, 15880-15886 (2008).

[58] C. Wang, et al., "Integrated lithium niobate electro-optic modulators operating at CMOS-compatible voltages," *Nature* **562**, 101 (2018).

[59] E. Sahin, K. J. A. Ooi, C. E. Png, and D. T. H. Tan, "Large, scalable dispersion engineering using cladding-modulated Bragg gratings on a silicon chip," *Applied Physics Letters* **110**, 161113 (2017).

[60] D. Liang, G. Roelkens, R. Baets, J. E. Bowers, "Hybrid integrated platforms for silicon photonics," *Materials* **3**, 1782-1802 (2010).

[61] B. Stern, X. Ji, Y. Okawachi, A. L. Gaeta, M. Lipson, "Battery-operated integrated frequency comb generator," *Nature* **562**, 401 (2018).

[62] H. Bao et al., "Laser Cavity-Soliton Micro-Combs", *Nature Photonics* vol. **13,** (6) 384–389 (2019).

[63] Maxwell Rowley, Pierre-Henry Hanzard, Antonio Cutrona, Hualong Bao, Sai T. Chu, Brent E. Little, Roberto Morandotti, David J. Moss, Gian-Luca Oppo, Juan Sebastian Totero Gongora, Marco Peccianti and Alessia Pasquazi, "Self-emergence of robust solitons in a micro-cavity", Nature **608**, (7922) 303 – 309 (2022).

DOI: 10.21203/rs.3.rs-468461/v1.

[64] Bao, C., et al., Direct soliton generation in microresonators, Opt. Lett, vol. 42, 2519 (2017).

[65] H Bao, L Olivieri, M Rowley, ST Chu, BE Little, R Morandotti, DJ Moss, ... "Turing patterns in a fiber laser with a nested microresonator: Robust and controllable microcomb generation", Physical Review Research vol. 2 (2), 023395 (2020).

[66] T. G. Nguyen et al., "Integrated frequency comb source-based Hilbert transformer for wideband microwave photonic phase analysis," Opt. Express, vol. 23, no. 17, pp. 22087-22097, Aug. 2015.

[67] X. Xu, et al., "Continuously tunable orthogonally polarized RF optical single sideband generator based on micro-ring resonators," Journal of Optics, vol. 20, no. 11, 115701. 2018.

[68] X. Xu, et al., "Orthogonally polarized RF optical single sideband generation and dual-channel equalization based on an integrated microring resonator," Journal of Lightwave Technology, vol. 36, no. 20, pp. 4808-4818. 2018.

[69] Xu, X., et al., Photonic microwave true time delays for phased array antennas using a 49 GHz FSR integrated micro-comb source, Photonics Research, vol. 6, B30-B36 (2018).

[70] M. Tan, X. Xu, J. Wu, T. G. Nguyen, S. T. Chu, B. E. Little, R. Morandotti, A. Mitchell, and D. J. Moss, "Photonic Radio Frequency Channelizers based on Kerr Optical Micro-combs", IOP Journal of Semiconductors Vol. 42 (4), 041302 (2021).

[71] M. Tan, X. Xu, J. Wu, T. G. Nguyen, S. T. Chu, B. E. Little, R. Morandotti, A. Mitchell, and D. J. Moss, "Orthogonally polarized Photonic Radio Frequency single sideband generation with integrated micro-ring resonators", IOP Journal of Semiconductors, Vol. 42 (4), 041305 (2021).

[72] C. Prayoonyong et al., "Frequency comb distillation for optical superchannel transmission", Journal of Lightwave Technology Vol. 39 (23) 7383-7392 (2021).

[73] M. Tan, et al., "Photonic RF and microwave filters based on 49GHz and 200GHz Kerr microcombs", Optics Communications vol. 465,125563, Feb. 22. 2020.

[74] X. Xu, et al., "Broadband photonic RF channelizer with 90 channels based on a soliton crystal microcomb", Journal of Lightwave Technology, Vol. 38, no. 18, pp. 5116 - 5121, 2020. doi: 10.1109/JLT.2020.2997699.

[75] X. Xu, et al., "Photonic RF phase-encoded signal generation with a microcomb source", J. Lightwave Technology, vol. 38, no. 7, 1722-1727, 2020.

[76] X. Xu, et al., "High performance RF filters via bandwidth scaling with Kerr micro-combs," APL Photonics, vol. 4, no. 2, pp. 026102. 2019.

[77] M. Tan, X. Xu, J. Wu, R. Morandotti, A. Mitchell, and D. J. Moss, "RF and microwave high bandwidth signal processing based on Kerr Micro-combs", Advances in Physics X, VOL. 6, NO. 1, 1838946 (2021).

[78] M. Tan, X. Xu, J. Wu, B. Corcoran, A. Boes, T. G. Nguyen, S. T. Chu, B. E. Little, R.Morandotti, A. Lowery, A. Mitchell, and D. J. Moss, ""Highly Versatile Broadband RF Photonic Fractional Hilbert Transformer Based on a Kerr Soliton Crystal Microcomb", Journal of Lightwave Technology, vol. 39 (24) 7581-7587 (2021).

[79] M. Tan, X. Xu, J. Wu, A. Boes, B. Corcoran, T. G. Nguyen, S. T. Chu, B. E. Little, R. Morandotti, A. Mitchell, and D. J. Moss, "Advanced applications of Kerr microcombs", Paper 11775-1. SPIE 11775, Integrated Optics: Design, Devices, Systems and Applications VI, (EOO21) OO107-8, Proc 1177504; Integrated Optics Conference, SPIE Optics and Optoelectronics Symposium, Prague, Czech Republic. April 19 - 22 (2021), doi.org/10.1117/12.2588733.

[80]   M. Tan et al., "RF and microwave fractional differentiator based on photonics", IEEE Transactions on Circuits and Systems II: Express Briefs Vol. 67 (11), 2767-2771 (2020).

[81] M. Ferrera et al., "CMOS compatible integrated all-optical RF spectrum analyzer", Optics Express, vol. 22, no. 18, 21488 - 21498 (2014).

[82] A. Pasquazi, et al., "Sub-picosecond phase-sensitive optical pulse characterization on a chip", Nature Photonics, vol. 5, no. 10, pp. 618-623 (2011).

[83] M. Kues, et al., "Passively modelocked laser with an ultra-narrow spectral width", Nature Photonics, vol. 11, no. 3, pp. 159, 2017.

[84] L. Razzari, et al., "CMOS-compatible integrated optical hyper-parametric oscillator," Nature Photonics, vol. 4, no. 1, pp. 41-45, 2010.

[85] M. Ferrera, et al., "Low-power continuous-wave nonlinear optics in doped silica glass integrated waveguide structures," Nature Photonics, vol. 2, no. 12, pp. 737-740, 2008.

[86] M.Ferrera et al., "On-Chip ultra-fast 1st and 2nd order CMOS compatible all-optical integration", Opt. Express, vol. 19, (23)pp. 23153-23161 (2011).

[87] D. Duchesne, M. Peccianti, M. R. E. Lamont, et al., "Supercontinuum generation in a high index doped silica glass spiral waveguide," Optics Express, vol. 18, no, 2, pp. 923-930, 2010.

[88] A. Pasquazi, et al., "All-optical wavelength conversion in an integrated ring resonator," Optics Express, vol. 18, no. 4, pp. 3858-3863, 2010.

[89] A. Pasquazi, Y. Park, J. Azana, et al., "Efficient wavelength conversion and net parametric gain via Four Wave Mixing in a high index doped silica waveguide," Optics Express, vol. 18, no. 8, pp. 7634-7641, 2010.

[90] M. Peccianti, M. Ferrera, L. Razzari, et al., "Subpicosecond optical pulse compression via an integrated nonlinear chirper," Optics Express, vol. 18, no. 8, pp. 7625-7633, 2010.

[91] Little, B. E. et al., "Very high-order microring resonator filters for WDM applications", IEEE Photonics Technol. Lett. 16, 2263–2265 (2004).

[92] M. Ferrera et al., "Low Power CW Parametric Mixing in a Low Dispersion High Index Doped Silica Glass Micro-Ring Resonator with Q-factor > 1 Million", Optics Express, vol.17, no. 16, pp. 14098–14103 (2009).

[93] M. Peccianti, et al., "Demonstration of an ultrafast nonlinear microcavity modelocked laser", Nature Communications, vol. 3, pp. 765, 2012.

[94] A. Pasquazi, et al., "Self-locked optical parametric oscillation in a CMOS compatible microring resonator: a route to robust optical frequency comb generation on a chip," Optics Express, vol. 21, no. 11, pp. 13333-13341, 2013.

[95] A. Pasquazi, et al., "Stable, dual mode, high repetition rate mode-locked laser based on a microring resonator," Optics Express, vol. 20, no. 24, pp. 27355-27362, 2012.

[96] Kues, M. et al. Quantum optical microcombs. Nature Photonics vol. 13, (3) 170-179 (2019).

[97] C. Reimer, L. Caspani, M. Clerici, et al., "Integrated frequency comb source of heralded single photons," Optics Express, vol. 22, no. 6, pp. 6535-6546, 2014.

[98] C. Reimer, et al., "Cross-polarized photon-pair generation and bi-chromatically pumped optical parametric oscillation on a chip", Nature Communications, vol. 6, Article 8236, 2015. DOI: 10.1038/ncomms9236.

[99] L. Caspani, C. Reimer, M. Kues, et al., "Multifrequency sources of quantum correlated photon pairs on-chip: a path toward integrated Quantum Frequency Combs," Nanophotonics, vol. 5, no. 2, pp. 351-362, 2016.

[100] C. Reimer et al., "Generation of multiphoton entangled quantum states by means of integrated frequency combs," Science, vol. 351, no. 6278, pp. 1176-1180, 2016.

[101] M. Kues, et al., "On-chip generation of high-dimensional entangled quantum states and their coherent control", Nature, vol. 546, no. 7660, pp. 622-626, 2017.

[102] P. Roztocki et al., "Practical system for the generation of pulsed quantum frequency combs," Optics Express, vol. 25, no. 16, pp. 18940-18949, 2017.

[103] Y. Zhang, et al., "Induced photon correlations through superposition of two four-wave mixing processes in integrated cavities", Laser and Photonics Reviews, vol. 14, no. 7, pp. 2000128, 2020. DOI: 10.1002/lpor.202000128

[104] C. Reimer, et al., "High-dimensional one-way quantum processing implemented on d-level cluster states", Nature Physics, vol. 15, no.2, pp. 148–153, 2019.

[105] A. Frigg, A. Boes, G. Ren, T.G. Nguyen, D.Y. Choi, S. Gees, D. Moss, A Mitchell, "Optical frequency comb generation with low temperature reactive sputtered silicon nitride waveguides", APL Photonics, Vol. 5 (1), 011302 (2020).

[106] D. J. Moss et al., "Tunable dispersion and dispersion slope compensators for 10Gb/s using all-pass multicavity etalons", IEEE Phot. Technology Letters, vol. 15, no. 5, 730-732 (2003).

[107] L. M. Lunardi, D.J. Moss, S.Chandrasekhar, L.L.Buhl, A. Hulse, P.Colbourne, G.Randall, S.Mclaughlin, "Tunable dispersion compensators based on multi-cavity all-pass etalons for 40Gb/s systems", Journal of Lightwave Technology Vol. 20, (12) 2136 (2002).

[108] R. C. Gonzalez, and R. E. Woods, "Digital Image Processing", New York: Addison-Wesley, (1993).
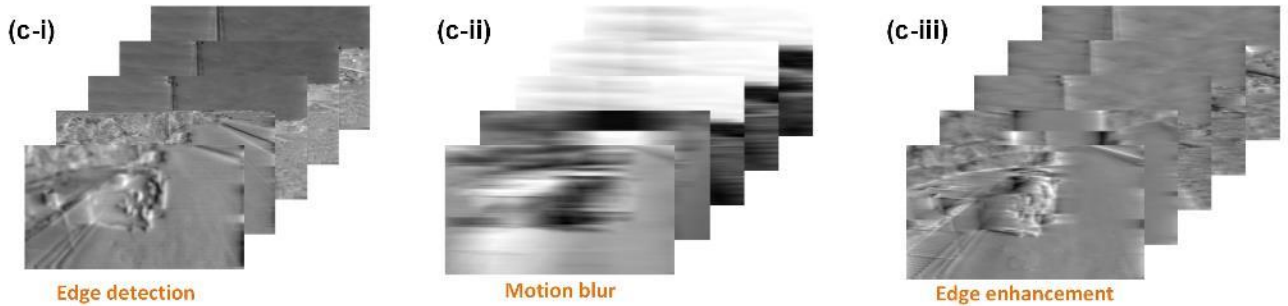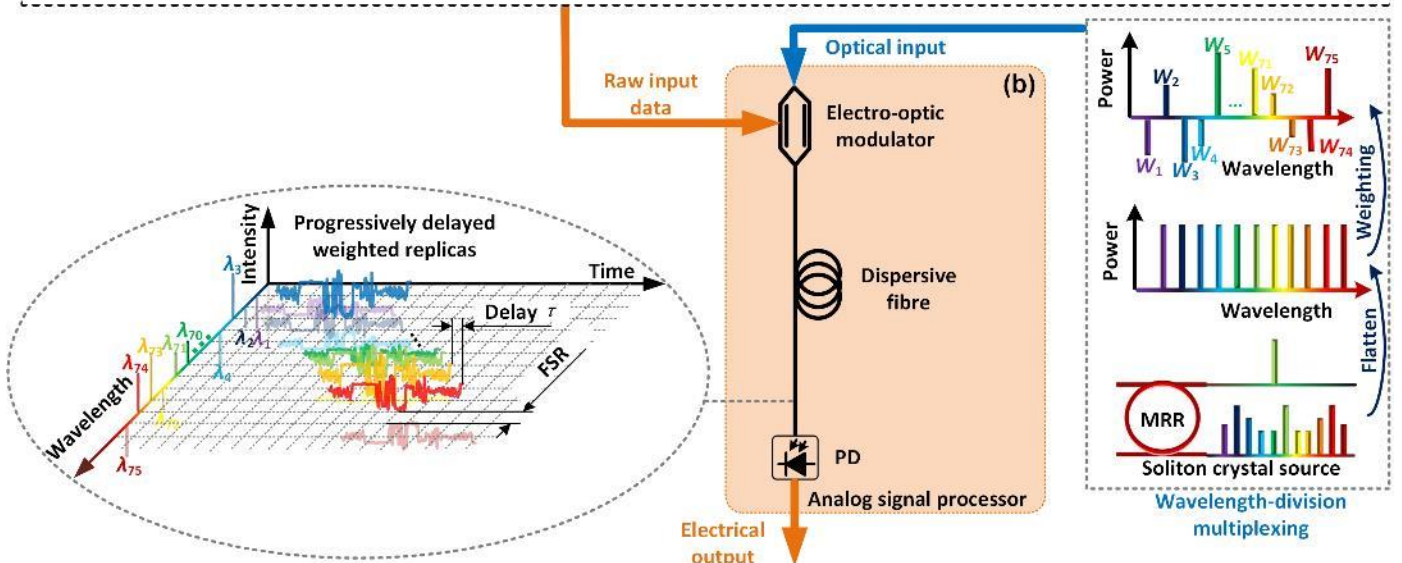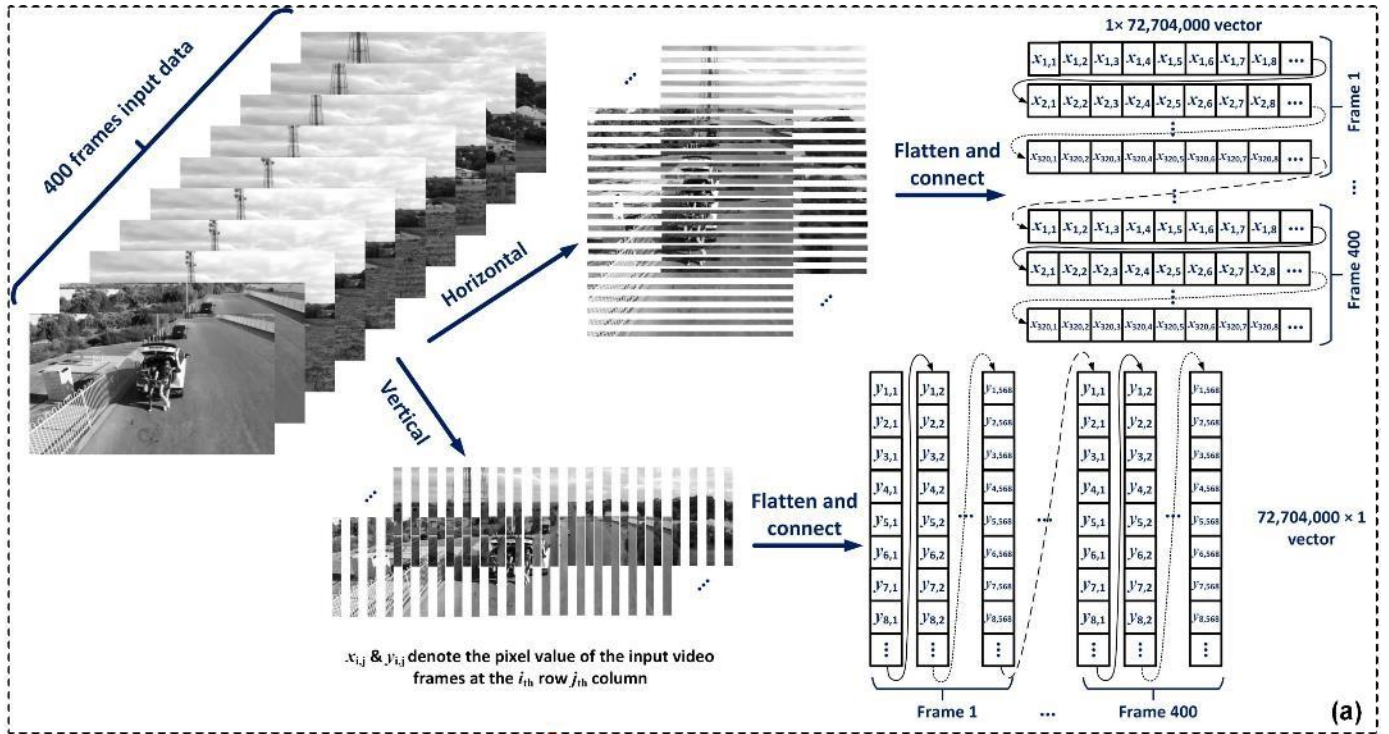
Figure 1. Operation principle of the RF photonic video image processor. PD: photodetector. (a) Diagram illustration of the flattening method applied to the input video frames. (b) Schematic illustration of experimental setup for video image processing. (c) The processed video frames after (i) 0.5 order differentiation for edge detection, (ii) integration for motion blue, and (iii) Hilbert transformation for edge enhancement.
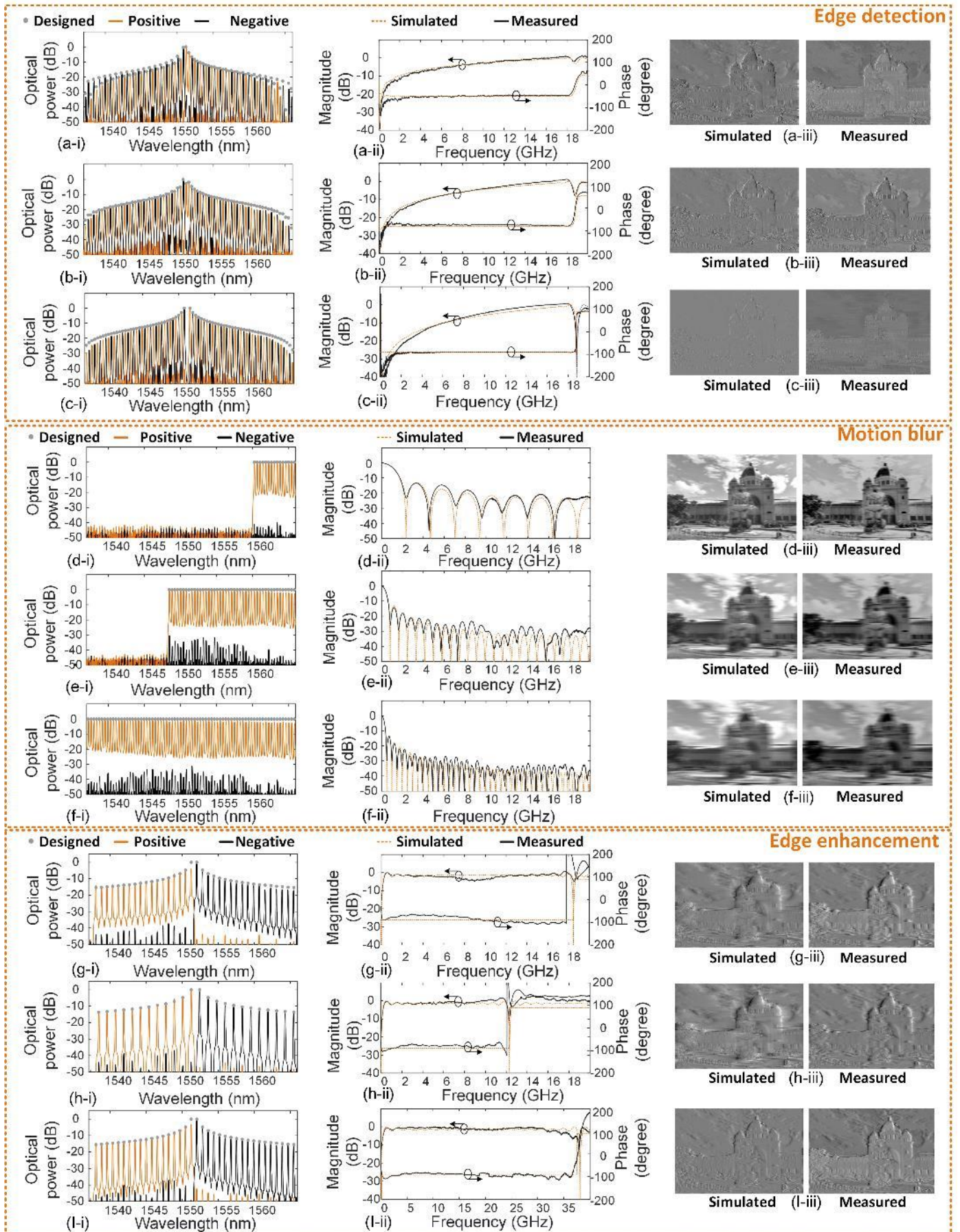
Figure 2. Experimental results of image processing. (a) – (c) Results for edge detection based on differentiation with order of 0.5, 0.75, and 1, respectively. (d) – (f) Results for motion blur based on integration with tap number of 15, 45, and 75, respectively. (g) – (I) Results for edge enhancement based on Hilbert transformation with operation bandwidth of 18 GHz, 12 GHz, and 38 GHz, respectively. In (a) – (I), (i) shows the designed and measured optical spectra of the shaped microcomb, (ii) shows the measured and simulated spectral response of the video image processing system, and (iii) shows the measured and simulated high definition (HD) video images after processing.
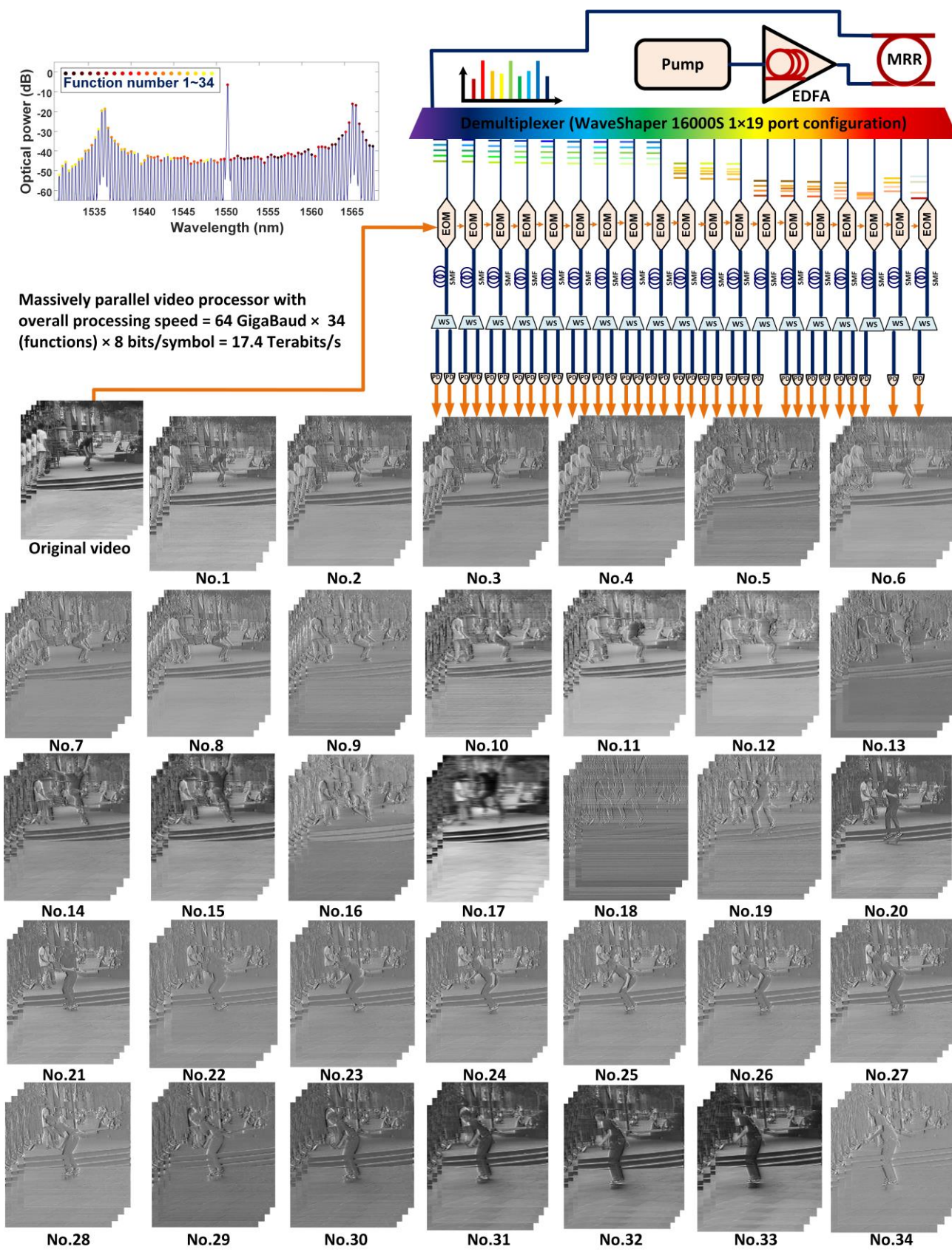
Figure 3. Massively parallel multi-functional video processing. EDFA: erbium doped fibre amplifier. MRR: micro-ring resonator. EOM: electro-optical Mach-Zehnder modulator. SMF: single-mode fibre. WS: WaveShaper. PD: photodetector. Detailed parameters for each function have been shown in Supp. Table S1.
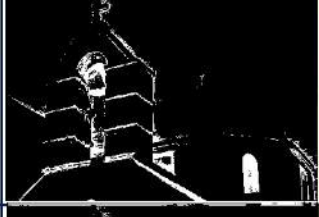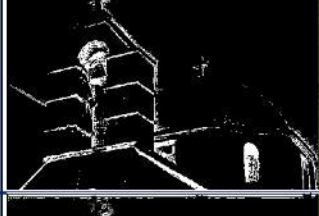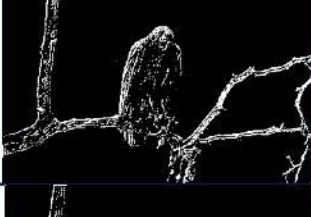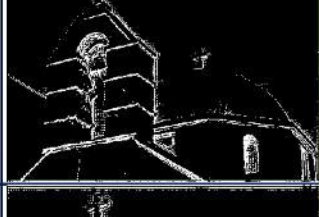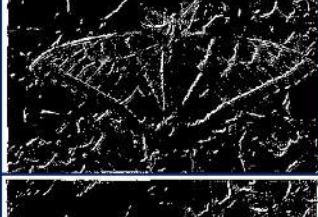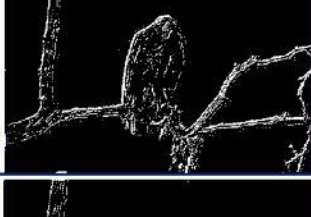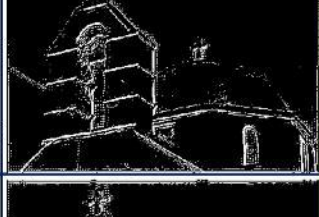
No.	118035	42049	35010
BSD Image			
Ground Truth			
Sobel			
Differentiation Order - 0.2			
Differentiation Order - 0.4			
Differentiation Order - 0.6			
Differentiation Order - 0.8			
Differentiation Order - 1.0			

Figure 4. Comparison of BSD images processed using the Sobel's algorithm and our video image processor after edge detection. Differentiation with different orders of 0.2, 0.4, 0.6, 0.8, and 1.0 are used for the edge detection with our video image processor.The Sobel results were performed electronically.
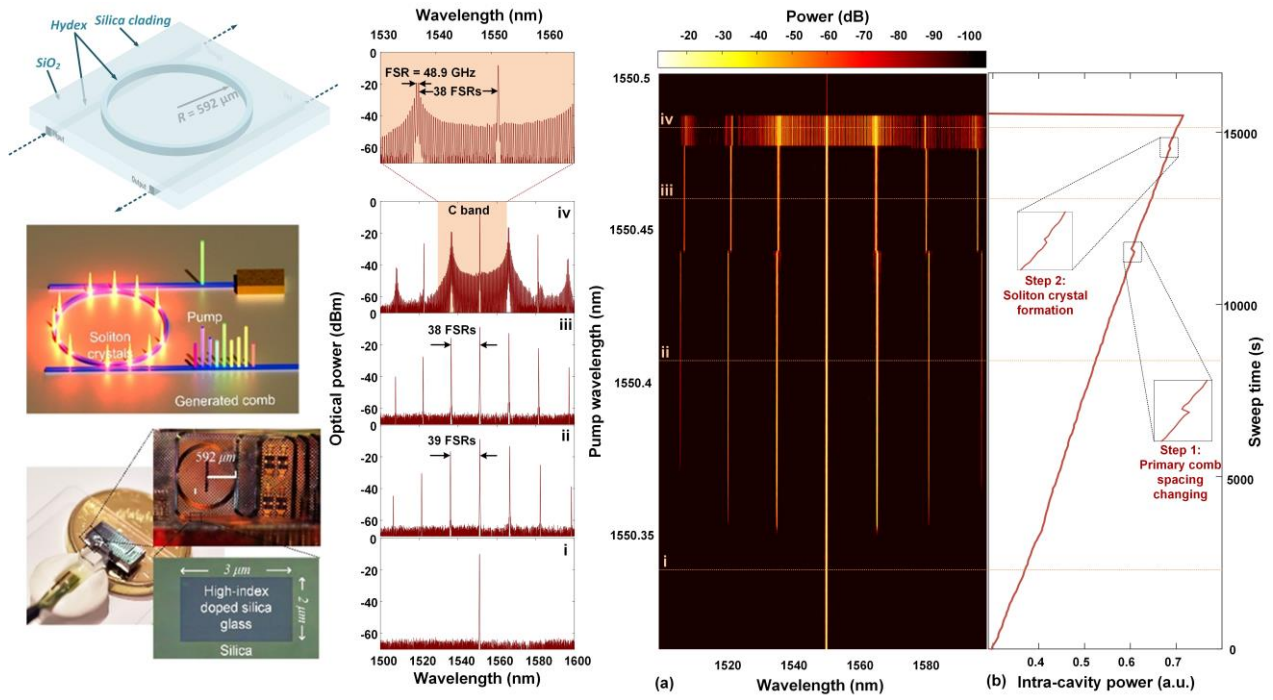
Extended data Figure 1. Soliton crystal (SC) microcomb used for video image processing. The SC microcomb is generated in a 4-port integrated micro-ring resonator (MRR) with an FSR of 48.9 GHz. Optical spectra of (i) Pump. (ii) Primary comb with a spacing of 39 FSRs. (iii) Primary comb with a spacing of 38 FSRs. (iv) SC micro-comb. (a) Optical spectrum of the micro-comb when sweeping the pump wavelength. (b) Measured soliton crystal step of the intra-cavity power.
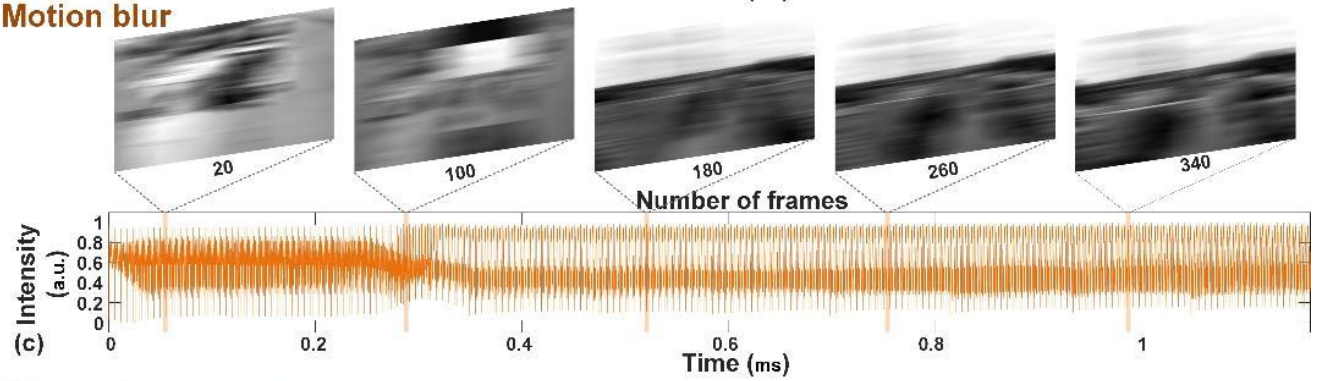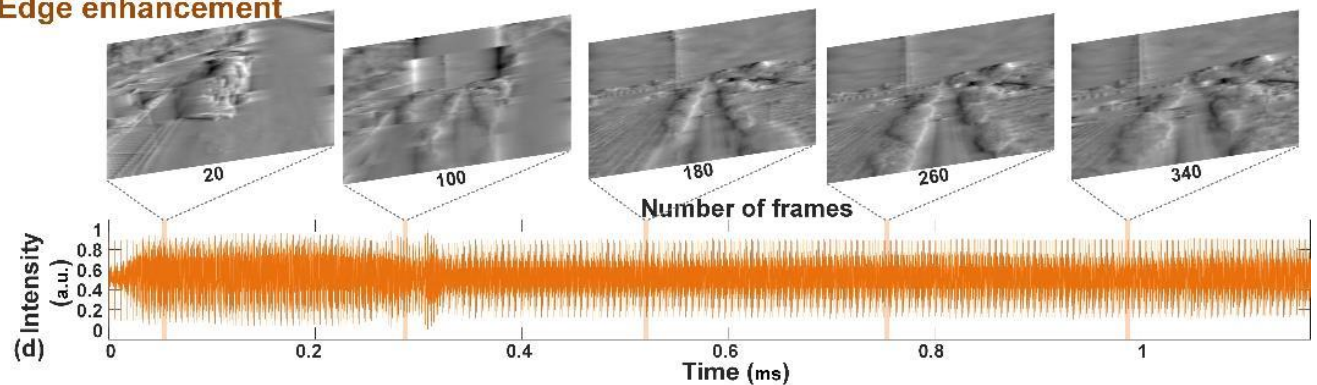
Original film
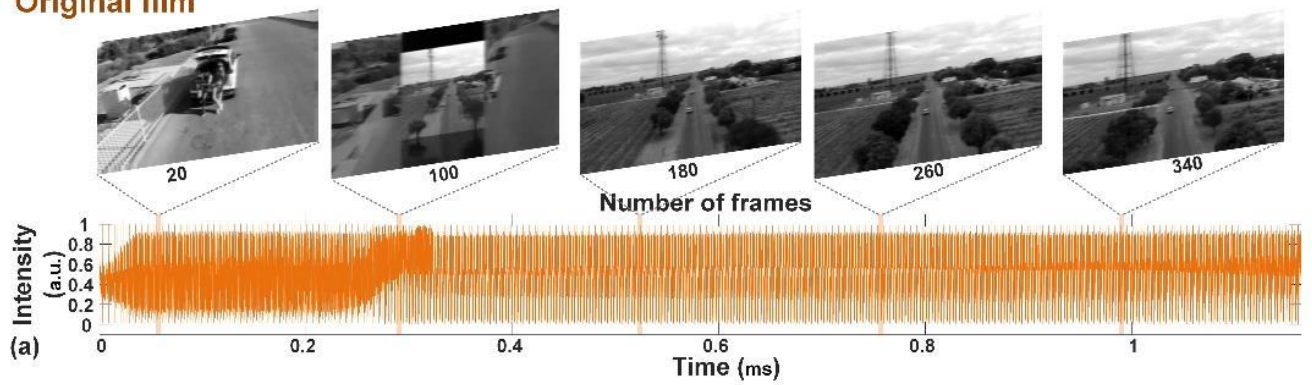
Edge detection
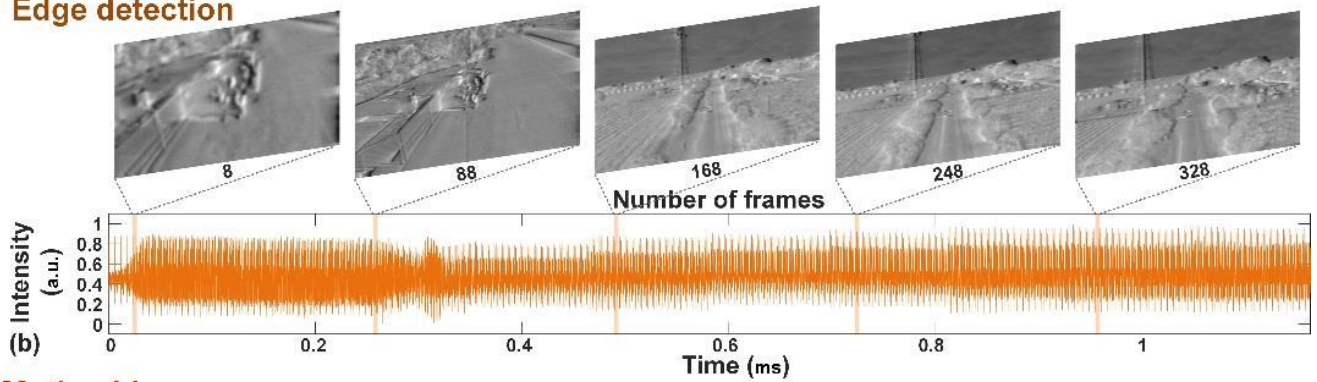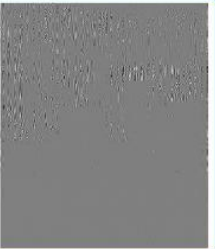
Motion blur

Edge enhancement

Extended data Figure 2. Measured video processing. (a) Original video. (b) Processed video after 0.5 order differentiation. (c) Processed video after integration. (d) Processed video after Hilbert transformation with 90-degree phase shift.

Frame no.30	1st order	2nd order	2.5th order	3rd order	5th order
Simulation					
Experiment					

Extended data Figure 3. Simulated and measured higher order derivatives.
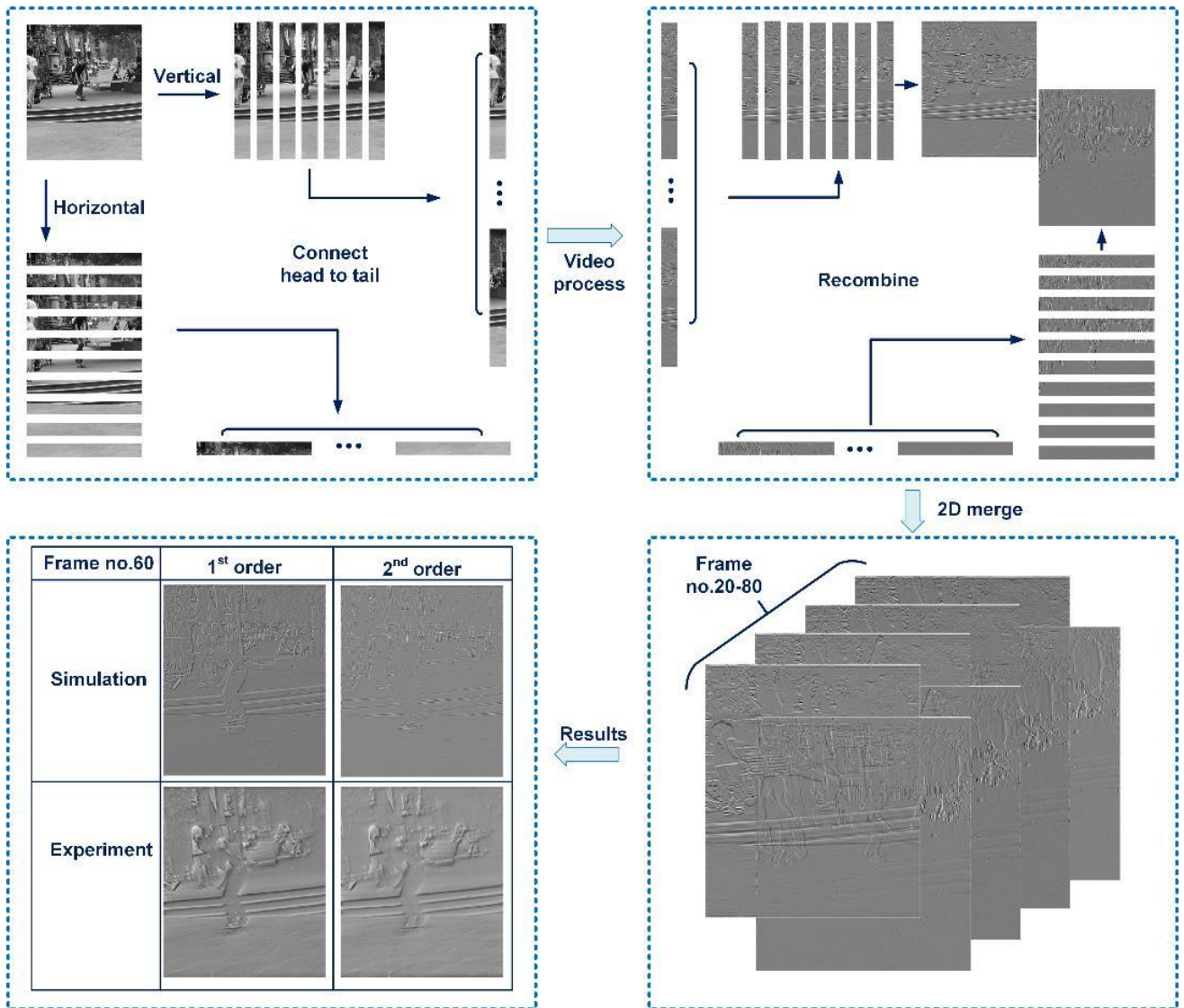
Extended data Figure 4. Illustration of two-dimensional derivative.

Table 1. Comparison of performance parameters of images processed using Sobel's algorithm and our video image processor.

BSD image No.	118035		42049		35010	
	PR	F-Measure	PR	F-Measure	PR	F-Measure
Sobel	12.2488	0.0068996	15.8362	0.0049214	11.3226	0.011988
Differentiation order – 0.2	12.7891	0.016586	20.1547	0.021603	18.3944	0.021787
Differentiation order – 0.4	13.629	0.014815	20.9594	0.024451	18.6818	0.022378
Differentiation order – 0.6	15.249	0.013748	21.0244	0.024771	19.8858	0.02388
Differentiation order – 0.8	16.2559	0.013491	21.4386	0.022484	20.0704	0.023491
Differentiation order – 1.0	17.4338	0.014391	22.1003	0.020635	20.6862	0.026481

Methods

Microcomb generation

We use SC microcombs generated by an integrated MRR (Fig. 1(a)) for video image processing. The SC microcombs, which include multiple self-organized solitons confined within the MRR, were also used for our previous demonstrations of RF photonic signal processing [40-44], ultra-dense optical data transmission [23], and optical neuromorphic processing [5, 45].

The MRR used to generate SC microcombs (Fig. 1(b)) was fabricated based on a complementary metal–oxide–semiconductor (CMOS) compatible doped silica glass platform [22-23]. It has a radius of ~592 μm, a high quality factor of ~1.5 million, and a free spectral range (FSR) of ~0.393 nm (i.e., ~48.9 GHz). The low FSR results in a large number of wavelength channels, which are used as discrete taps in our RF photonic transversal filter system for video image processing. The cross-section of the waveguide was 3 μm × 2 μm, resulting in anomalous dispersion in the C-band (Supplementary Fig. S1). The input and output ports of the MRR were coupled to a fibre array via specially designed mode converters, yielding a low fibre-chip coupling loss of 0.5 dB/facet.

In our experiment, a continuous-wave (CW) pump light was amplified to 30.5 dBm and the wavelength was swept from blue to red. When the detuning between pump wavelength and MRR's cold resonance became small enough, the intra-cavity power reached a threshold, and optical parametric oscillation driven by modulation instability (MI) was initiated. Primary combs (Fig. 1 (d-ii) and (d-iii)) were first generated, with the comb spacing determined by the MI gain peak [22, 24]. As the detuning changed further, a second jump in the intra-cavity power was observed, where distinctive 'fingerprint' SC comb spectra (Fig. 1 (d-iv)) appeared, with a comb spacing equal to the MRR's FSR. The SC microcomb arising from spectral interference between the tightly packaged solitons circulating along the ring cavity exhibits high coherence and low RF intensity noise (Fig. 1(c)), which are consistent with our simulations (Supplementary Movie S1). It is also worth mentioning that the SC microcomb is highly stable with only open-loop temperature control (Supplementary Fig. S2). In addition, it can be generated through manual adiabatic pump wavelength sweeping – a simple and reliable initiation process that also results in much higher energy conversion efficiency than single-soliton states [5, 23].

Microcomb shaping approach

To achieve the designed tap weights, the generated SC microcomb was shaped in power using liquid crystal on silicon (LCOS) based spectral WaveShapers. We used two-stage comb shaping in the video image processing experiments. The generated SC microcomb was pre-flattened and split by the first WaveShaper (Finisar 16000S), which yields an improved optical signal-to-noise ratio (OSNR) and a reduced loss control range for the second-stage comb shaping. The pre-flattened and split comb was then accurately shaped by the second WaveShaper (Finisar 4000S) according to the designed tap coefficients for different video image processing functions. The positive and negative tap coefficients were achieved by separating the wavelength channels into two spatial outputs of the second WaveShaper and then detected by a balanced photodetector (Finisar BPDV2150R).

In order to improve the comb shaping accuracy, a feedback control loop was employed for the second WaveShaper. First, we used RF Gaussian pulses as the system input and measured replicas of the input pulses in different wavelength channels. Next, we extracted peak intensities of the system impulse response and obtained accurate RF-to-RF tap coefficients. Finally, the extracted tap coefficients were subtracted from the ideal tap coefficients to obtain an error signal, which was used to calibrate the loss of the second WaveShaper. After several iterations of the comb shaping loop, an accurate impulse response that compensated for the non-ideal impulse response of the system was obtained, thus significantly improving the accuracy of the RF photonic video image processing. Directly measuring the system impulse response is more accurate compared to measuring the optical power of the comb lines, given the slight difference between the two ports into the balanced detector. The shaped impulse responses for different image processing functions are shown in the Supplementary Figs. S3 – S6.

Derivative (from fractional to high order)

The transfer function of a differentiator is given by

$$H(\omega) \propto (j\omega)^N \tag{2}$$

where j equals to $\sqrt{1}$, ω represents the angular frequency, and N is the order of differentiation, which in our case can be both fractional [40, 47, 78, 80] and integral [18], and even complex. The experiment results for both fractional and integral order differentiation can be seen in Supplementary Movie S2. The fractional-order is tunable from 0.05 to 1.1, with a step of 0.05. We achieved high order differentiation with an order of 2, 2.5, 3, which to the best of our knowledge, is the highest order of derivative that can be achieved for video image processing.

Two-dimensional video image processing

Normally, processing functions such as differentiation, operating on video signals, only result in a one dimensional process – since it acts on individual lines of the video raster image. However, by appropriately pre-processing the video signal it is possible to obtain a fully two-dimensional derivative [108]. $f_z(x, y)$ represent the z_{th} frame of a video signal with $M \times N$ pixels, where $x = 0, 1, 2, \dots , M - 1, y = 0, 1, 2, \dots , N - 1$. Thus, the two-dimensional derivative result is given by:

$$D_z(\mathrm{u}, \mathrm{v}) = \sum_{n=0}^{N-1} h_x(n)e^{-j\omega_x nT} \sum_{n=0}^{N-1} h_y(n)e^{-j\omega_y nT} \tag{3}$$

where N is the number of taps, $u = 0, 1, 2, \dots , M - 1, v = 0, 1, 2, \dots , N - 1$.

The electrical input data was temporally encoded by an arbitrary waveform generator (Keysight M8195A). The raw input matrices were first sliced horizontally and vertically into multiple rows and columns, respectively, which were flattened into vectors and connected head-to-tail. After that, the generated vectors were multicast onto different wavelength channels via a 40-GHz intensity eletro-optic modulator (iXblue). For the video with a resolution of 303×262 pixels and a frame rate of 30 frames per second, we used a sampling rate of 64 Giga samples/s to form the input symbols. A dispersive fibre was employed to provide a progressive delay T. Next, the electrical output waveform was resampled and digitized by a high-speed oscilloscope (Keysight DSOZ504A) to generate the final output. The magnitude and phase responses of the RF photonic video image processing system were characterized by a vector network analyser (Agilent MS4644B 40 GHz bandwidth) working in the S21 mode. Finally, we restored the processed video into the original size of the matrix and took the average of horizontally and vertically processed video and formed this into a two-dimensional processed video (Supplementary Movie S2).

Details of the video image dataset

The high definition (HD) image with a resolution of 1080×1620 pixels we performed is a photo taken by Nikon D5600 in front of the Exhibition building in the centre of Melbourne city, Australia, in 2020. The video of 568×320 pixels was captured by a Drone Quadcopter UAV with Optical Zoom camera (DJL Mavic Air2 Zoom), this was a short trip during the eastern holiday, in 2019. The author and her friend were started from Melbourne to Adelaide, passing the pink lake and playing guitar, this was a great memory before the pandemic and continuous lockdown in Melbourne. The short video of the skateboard with a resolution of 303×262 pixels was taken by the author using iPhone SE in front of Victoria Library, Melbourne, Australia, in 2020.